1-1-2023

CLEAR: Spatially Resolved Emission Lines and Active Galactic Nuclei at 0.6 < z < 1.3

Bren E. Backhaus

Joanna S. Bridge

Jonathan R. Trump

Nikko J. Cleri

Casey Papovich

See next page for additional authors

Original Publication Information
Bren E. Backhaus *et al* 2023 *ApJ* 943 37. DOI 10.3847/1538-4357/aca668

The Astrophysical Journal, 943:37 (14pp), 2023 January 20 https://doi.org/10.3847/1538-4357/aca668

CLEAR: Spatially Resolved Emission Lines and Active Galactic Nuclei at $0.6 < z < 1.3$

Bren E. Backhaus[1,2], Joanna S. Bridge[3], Jonathan R. Trump[1], Nikko J. Cleri[1,4,5], Casey Papovich[4,5], Raymond C. Simons[2], Ivelina Momcheva[2,6], Benne W. Holwerda[3], Zhiyuan Ji[7], Intae Jung[8], and Jasleen Matharu[4,5,9]
[1] Department of Physics, University of Connecticut, 196 Auditorium Road, Unit 3046, Storrs, CT 06269, USA
[2] Space Telescope Science Institute, 3700 San Martin Drive, Baltimore, MD 21218 USA
[3] Department of Physics and Astronomy, University of Louisville, 102 Natural Science Building, Louisville, KY 40292, USA
[4] Department of Physics and Astronomy, Texas A&M University, College Station, TX 77843-4242, USA
[5] George P. and Cynthia Woods Mitchell Institute for Fundamental Physics and Astronomy, Texas A&M University, College Station, TX 77843-4242, USA
[6] Max-Planck-Institut für Astronomie, Königstuhl 17, D-69117 Heidelberg, Germany
[7] University of Massachusetts Amherst, 710 North Pleasant Street, Amherst, MA 01003-9305, USA
[8] Astrophysics Science Division, Goddard Space Flight Center, Greenbelt, MD 20771, USA
[9] Cosmic Dawn Center, Niels Bohr Institute, University of Copenhagen, Rådmandsgade 62, 2200 Copenhagen, Denmark
Received 2022 July 20; revised 2022 October 24; accepted 2022 November 24; published 2023 January 23

Abstract

We investigate spatially resolved emission-line ratios in a sample of 219 galaxies ($0.6 < z < 1.3$) detected using the G102 grism on the Hubble Space Telescope Wide Field Camera 3 taken as part of the CANDELS Lyα Emission at Reionization survey to measure ionization profiles and search for low-luminosity active galactic nuclei (AGN). We analyze [O III] and Hβ emission-line maps, enabling us to spatially resolve the [O III]/Hβ emission-line ratio across the galaxies in the sample. We compare the [O III]/Hβ ratio in galaxy centers and outer annular regions to measure ionization differences and investigate the potential of sources with nuclear ionization to host AGN. We investigate some of the individual galaxies that are candidates to host strong nuclear ionization and find that they often have low stellar mass and are undetected in X-rays, as expected for low-luminosity AGN in low-mass galaxies. We do not find evidence for a significant population of off-nuclear AGN or other clumps of off-nuclear ionization. We model the observed distribution of [O III]/Hβ spatial profiles and find that most galaxies are consistent with a small or zero difference between their nuclear and off-nuclear line ratios, but 6%–16% of galaxies in the sample are likely to host nuclear [O III]/Hβ that is ∼0.5 dex higher than in their outer regions. This study is limited by large uncertainties in most of the measured [O III]/Hβ spatial profiles; therefore, deeper data, e.g., from deeper HST/WFC3 programs or from JWST/NIRISS, are needed to more reliably measure the spatially resolved emission-line conditions of individual high-redshift galaxies.

Unified Astronomy Thesaurus concepts: Galaxies (573); Active galaxies (17); Emission line galaxies (459)

Supporting material: machine-readable table

1. Introduction

The rest-frame optical spectra of galaxies can be used to infer a wide variety of physical properties via their nebular and recombination lines to determine, for example, star formation rate (SFR; e.g., Kennicutt 1998; Kennicutt & Evans 2012), metallicity (e.g., Pagel & Edmunds 1981; Zahid et al. 2013; Maiolino & Mannucci 2019), interstellar medium density (Kewley et al. 2019), temperature (e.g., Peimbert et al. 2017), and dust attenuation (e.g., Cardelli et al. 1989; Calzetti 2001). Additionally, emission-line ratios have been used to identify active galactic nuclei (AGN), such as the [N II]/Hα and [O III]/Hβ ratios used in the "BPT"[9] diagram (Baldwin et al. 1981; Veilleux & Osterbrock 1987; Kewley et al. 2001; Kauffmann et al. 2003), the mass-excitation (MEx) diagram (Juneau et al. 2011), and the [O III]/Hβ versus [Ne III]/[O II] (OHNO) "OHNO" diagram (Backhaus et al. 2022). Narrow-line AGN selection methods are particularly important because they are complementary to multiwavelength AGN selections; different methods have different biases as a function of host galaxy properties and/or AGN Eddington ratio (Hickox et al. 2009; Aird et al. 2012; Trump et al. 2013, 2015; Buchner et al. 2015; Jones et al. 2016; Cann et al. 2019; Lambrides et al. 2020; Ji et al. 2022).

Determining the physical conditions of galaxies around the peak of cosmic star formation ($z \sim 2$) is complicated. At these redshifts, optical diagnostic lines such as [O III]λ5007+λ4959 and Hα are redshifted into the infrared, where atmospheric opacity and high background make ground-based observations challenging. Additionally, interpreting BPT diagrams at higher redshifts is complicated by higher SFRs (Madau & Dickinson 2014) and harder ionizing radiation (Steidel et al. 2014; Kewley et al. 2015), making it difficult to distinguish ionization from an AGN and from high-redshift star formation processes (Moran et al. 2002; Coil et al. 2015; Trump et al. 2015). This is especially true in low-mass galaxies, where X-ray detection of AGN is unlikely (Xue et al. 2010; Aird et al. 2012).

Spatially resolved lines can be used to gather further information on galaxy evolution and formation. Spatially resolving Hα gives the profile of star formation within a galaxy. This gives us information about whether a galaxy is formed inside-out or outside-in by comparing to the galaxy's stellar continuum (Nelson et al. 2012, 2016a, 2021; Matharu et al. 2022). Spatially resolving the Balmer decrement (Hα/Hβ) measures the

[9] Baldwin, Phillips, and Terlevich.

profile of dust attenuation within a galaxy. In low-mass galaxies at redshifts $z \sim 1.4$, the dust attenuation gradients have been measured to be relatively flat, on average (Nelson et al. 2016b). As mass increases, dust attenuation increases toward the center of the galaxy (Nelson et al. 2016b).

Spatially resolving the [O III]/Hβ line ratio has shown promise for decomposing nuclear AGN and extended star formation activity. Trump et al. (2011) and Wright et al. (2010) examined stacked Wide Field Camera 3 (WFC3) G141 grism spectra and found that elevated central [O III]/Hβ ratios may indicate the presence of obscured or dim AGN. Using simulations of two-orbit WFC3/G141 grism observations, Bridge et al. (2016) showed that it is possible to detect low-luminosity AGN in individual galaxies, particularly low-mass galaxies, by spatially resolving the [O III]/Hβ line ratio in the inner and outer regions of the galaxy using the G141 spectrum. That study made use of the MEx diagnostic diagram (Juneau et al. 2011, 2014) in order to distinguish between AGN and star formation activity. The MEx diagram replaces the [N II]/Hα axis of the traditional BPT diagram with stellar mass. The mass–metallicity relation has shown that there is a correlation between mass and [N II]/Hα (e.g., Tremonti et al. 2004), facilitating the use of this diagnostic even when the [N II] and Hα lines are not available.

In order to address the challenges of understanding high-redshift emission-line galaxies, the WFC3 (Kimble et al. 2008) G102 ($0.8\ \mu\mathrm{m} < \lambda < 1.15\ \mu\mathrm{m}$, $R \sim 210$) and G141 ($1.1\ \mu\mathrm{m} < \lambda < 1.7\ \mu\mathrm{m}$, $R \sim 130$) slitless grisms on the Hubble Space Telescope (HST) have been used to conduct large surveys of thousands of galaxies in the near-infrared regime. These surveys have expanded our understanding of the physical conditions of galaxies since cosmic noon (e.g., the 3D-HST survey, Momcheva et al. 2016; and the Faint Infrared Grism Survey, FIGS, Pirzkal et al. 2017).

In this work, we investigate the spatially resolved [O III]/Hβ emission-line profiles of 219 galaxies at redshift $z \sim 0.9$ observed by the CANDELS Lyα Emission at Reionization (CLEAR) survey. We use the spatially resolved emission-line ratios to infer the ionization profiles of the galaxies and particularly search for nuclear ionization in low-mass galaxies in order to identify low-luminosity AGN that are typically missed by X-ray detection. We also compare galaxy ionization profiles to other galaxy properties, such as stellar mass, SFR, effective radius, and redshift.

In Section 2, we describe the observations and data reduction. In Section 3, we explain our sample selection, and in Section 4, we discuss our method for spatially resolving the [O III]/Hβ line ratio. Section 5 describes how the spatially resolved [O III]/Hβ emission line relates to different galaxy properties. We discuss the spatially resolved [O III]/Hβ's ability to detect low-luminosity AGN and regions of higher ionization in Section 6. We present our conclusions in Section 7. Throughout this paper, we assume a ΛCDM cosmology with $H_0 = 70$ km s^{-1} Mpc^{-1}, $\Omega_m = 0.3$, and $\Omega_\Lambda = 0.7$ (Planck Collaboration et al. 2016).

2. Observations and Data Reduction

The data used in this work are comprised of HST/WFC3 G102 grism ($0.8\ \mu\mathrm{m} < \lambda < 1.15\ \mu\mathrm{m}$) observations from various surveys, the majority of which were taken as part of the CLEAR (Estrada-Carpenter et al. 2019) G102 grism survey. The G102 observations come from programs GO-14227 (PI: C. Papovich), GO-13420 (PI: G. Barro), and GO/DD-11359 (ERS; PI: R. O'Connell). The HST/WFC3 also has G141 observations that come from programs GO-11600 (AGHAST; PI: B. Weiner), GO-12461 (SN Colfax; PI: A. Reiss), GO-13871 (PI: P. Oesch), GO/DD-11359 (ERS; PI: R. O'Connell), GO-12099 (George, Primo; PI: A. Reiss), and GO-12177 (3D-HST; PI: van Dokkum). CLEAR includes six pointings in the CANDELS (Koekemoer et al. 2011) Great Observatories Origin Deep survey (GOODS)-North (GN) field with a 10-orbit depth and six pointings in the GOODS-South (GS) field with a 12-orbit depth. These data sets provide low-resolution grism spectroscopy over observed-frame $0.8\ \mu\mathrm{m} < \lambda < 1.65\ \mu\mathrm{m}$ for every source in the field of view, with $R \sim 210$ in G102. The CLEAR pointings overlap with the 3D-HST survey (Momcheva et al. 2016), which gives G141 slitless grism spectra covering 1.1–1.65 μm with a two-orbit depth that were used in the data reduction to aid in redshift determination. In contrast to the low spectral resolution, the 2D spectra have a high spatial resolution of $0\farcs06$ pixel^{-1}.

The CLEAR survey is augmented by G102 observations from FIGS (HST-GO 13776; PI: Malhotra). The FIGS campaign is comprised of four pointings of 40-orbit observations in the GOODS fields (see Tilvi et al. 2016), one of which overlaps with a CLEAR pointing in GS. This pointing was therefore also ingested into the CLEAR data. The FIGS data were reduced and processed in the same fashion as the CLEAR data (Section 2.2).

The CLEAR spectra have been used to study the metallicities, ages, and formation histories of massive high-redshift galaxies (Estrada-Carpenter et al. 2019, 2020; Simons et al. 2021) and appraise Paschen-β as an SFR indicator in low-redshift galaxies (Cleri et al. 2022). Matharu et al. (2022) used spatially resolved Hα emission-line maps of star-forming galaxies to study the evolution of gradients in galaxy assembly. Jung et al. (2022) used CLEAR to study the evolution of the strength of Lyα emission at $6.5 < z < 8.2$. Backhaus et al. (2022) and Papovich et al. (2022) used CLEAR spectra to study the physical conditions of galaxies and their (spatially integrated) gas conditions.

The HST data used in this paper can be found in MAST: 10.17909/t9-ctff-wx60.

2.1. CLEAR Observing Strategy

The CLEAR observations were taken over the course of 2 yr (2015 November to 2017 February). Direct imaging observations were done using the WFC3 F105W filter. Each field was observed with three different orients. Each orient in the GS field has four orbits and the GN field has two orients with four orbits with a single orient with two orbit depth. These orients are separated by $\sim 10°$–$20°$ in roll angle to facilitate the separation of overlapping spectra.

The Earth's atmosphere produces a time-variable background caused by He I emission at 10830 Å that affects both the F105W filter and the G102 grism. The observations were scheduled to reduce this background by placing the G102 grism observations during times of low background and the F105W observations when the background is predicted to be higher in order to minimize the background in the spectra (see Brammer et al. 2014; Tilvi et al. 2016; Lotz et al. 2017 for further information).

2.2. Spectroscopic Data Reduction

The G102 grism data from all of the surveys were reduced together using the grism redshift and line analysis software `grizli` (Brammer 2022). The complete reductions are

described in detail in Simons et al. (2021), but we describe the process briefly here. CLEAR F105W reference images and the dispersed G102 grism were aligned to the same world coordinate system as the 3D-HST photometric catalog (Skelton et al. 2014). Cosmic-ray cleaning, flat-fielding, and sky subtraction (using WFC3/IR master sky images; Brammer et al. 2015) were then performed.

Contamination from overlapping spectra is a known issue in grism spectroscopy. It is more significant for faint sources contaminated by bright ones because subtracting bright sources from faint spectra introduces errors and contributes residual flux to the spectra of faint sources. The continuum models of these overlapping sources are subtracted from object spectra. The contamination of the 2D spectra was modeled in two steps. First, a flat continuum model was used for objects down to $m_{\rm F105W} < 25$. Subsequently, a polynomial continuum was used for objects with $m_{\rm F105W} < 24$. All objects with $m_{\rm F105W} < 25$ were then extracted from the CLEAR imaging, with 2D spectral extractions for each grism observation, for about 6000 extracted objects.

Fits to the spectra were carried out with `grizli` using the CLEAR F105W images, as well as the photometry available from 3D-HST (Skelton et al. 2014). In order to determine the redshift of each object, flexible stellar population synthesis (FSPS) stellar population models (Conroy & Gunn 2010) were used with fixed emission-line sets and ratios. Line fluxes were then determined using the best-fit redshift.

The `grizli` software creates spatially resolved emission-line maps by fitting a model to the 2D spectrum of the object of interest and subtracting the continuum. The line maps for each emission line present in the spectrum are then created by drizzling the best-fit galaxy model at the wavelength of each emission line in the spectrum. This results in a 2D map with a pixel scale of $0\farcs1 \times 0\farcs1$ of the flux that is in excess of the continuum at each line wavelength.

3. Sample Selection

The final CLEAR catalog (Simons et al., in preparation) contains the 1D and 2D spectra, total (integrated) line fluxes, and emission-line maps of more than 6000 objects. We implemented a cut in the grism redshift fits to require $(z_{97} - z_{02})/2 < 0.005$ to ensure robust line identification, where z_{97} and z_{02} are the 97th and 2nd percentiles of the redshift probability distribution produced by `grizli` for each object.

We focus on the [O III]/Hβ ratio (with air wavelengths of 5007 and 4861 Å, respectively) that is ideal for detection with the G102 grism. This ratio has been identified as a tracer of AGN activity (e.g., Baldwin et al. 1981; Juneau et al. 2014; Bridge et al. 2016) because a high [O III]/Hβ ratio indicates the presence of the harder ionizing radiation necessary to produce [O III] oxygen (Kewley et al. 2015). Additionally, the fact that the [O III] doublet and Hβ are close in wavelength makes their ratio nearly independent of extinction. Requiring multiple line pairs (such as [Ne III]/[O II] or [S II]/Hα) would significantly reduce the redshift range and sample size.

We then use the integrated [O III] and Hβ line fluxes (total fluxes integrated across a whole galaxy) to impose a signal-to-noise ratio (S/N) cut on the [O III]/Hβ emission-line ratio of $S/N_{\rm [O\,III]/\beta} > 3/\sqrt{2}$, the low end of which is equivalent to both lines being measured at exactly 3σ. An S/N cut on the ratio allows for the inclusion of objects where one line may be less well measured than the other. Since Hβ is generally weaker than [O III] in our galaxies, selecting based on the S/N of the ratio rather than each line also makes our sample less biased to lower [O III]/Hβ ratios. The minimum S/N for the sample is S/N > 2.2 for Hβ and S/N > 2.7 for [O III]. That said, we repeated our analysis on a sample selected by S/N > 3 in each emission line and found similar results to our current sample, with slightly larger uncertainties due to the smaller (by ∼20%) sample size.

Finally, we examine both the 1D spectra and 2D emission-line maps by eye to ensure a robust sample of galaxies with well-determined [O III]/Hβ ratios. In some cases, errors in the continuum model leave unphysical artifacts in the emission-line maps. We remove these objects from the sample to include only those with well-fit continua. This removes ∼28% of our sample, leaving our final sample to contain 219 emission-line objects. The Hβ SFR and stellar mass distribution of our sample compared to the entire CLEAR sample at $0.6 < z < 1.3$ is shown in Figure 1. The SFR is calculated from the attenuation-corrected Hβ luminosity using the Kennicutt & Evans (2012) SFR relation with an intrinsic Hα/Hβ = 2.86 (assuming Case B recombination, $T = 10^4$ K, and $n_e = 10^4$ cm^{-3}; Osterbrock & Miller 1989) and a Calzetti (2001) attenuation curve:

$$\log(\mathrm{SFR})[M_\odot\ \mathrm{yr}^{-1}] = \log[L(\mathrm{H}\beta)] - 40.82. \quad (1)$$

The star formation mass sequence line is from Whitaker et al. (2012) using the sample's average redshift of $z = 1.0$:

$$\begin{aligned} &\log(\mathrm{SFR})[M_\odot\ \mathrm{yr}^{-1}] = \alpha(z)(\log(M_*) - 10.5) + \beta(z) \\ &\alpha(z) = (0.7\text{–}0.13z) \\ &\beta(z) = 0.38 + 1.14z\text{–}0.19z^2. \end{aligned} \quad (2)$$

3.1. Stellar Masses

Following the method of Estrada-Carpenter et al. (2019), the stellar masses were determined using `eazy-py` (Brammer 2021), a spectral energy distribution fitting package based on the photometric redshift fitting code `EAZY` (Brammer et al. 2008). The algorithm uses 12 FSPS templates, each with their own unique star formation history. The templates all use a Chabrier initial mass function (Chabrier 2003).

3.2. X-Ray Counterparts

We matched objects in our sample with known X-ray-emitting counterparts in the Chandra Deep Fields using the the 2 Ms CDF-N (Xue et al. 2016) and 7 Ms CDF-S (Luo et al. 2017) point-source catalogs. Any galaxy from the CLEAR sample that corresponds to an optical counterpart in the X-ray source catalogs within $0\farcs5$ is considered an X-ray object. Two counterparts were classified as X-ray galaxies (i.e., X-ray emission consistent with X-ray binaries and other processes associated with star formation), and 11 objects were classified as X-ray AGN. These classifications were made based on the strength and hardness of the galaxies' X-ray flux (see Xue et al. 2016 and Luo et al. 2017 for details).

4. Spatially Resolved Line Ratios

We use the 2D line maps to measure the spatially resolved emission lines from each galaxy. We are specifically interested in the [O III]/Hβ line ratio, and we use the line maps (examples of which are shown in Figure 2) to measure differences in the

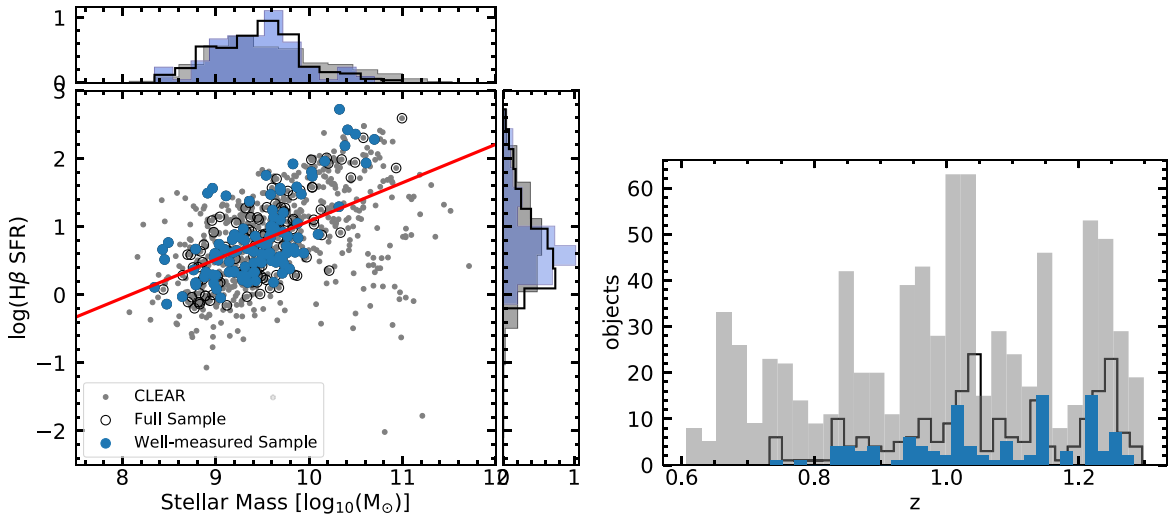

Figure 1. Left: distribution of stellar mass and Hβ SFR from our selected sample of CLEAR galaxies in the range $0.6 < z < 1.3$, color-coded by redshift, compared to the complete CLEAR data set in the range $0.6 < z < 1.3$ (gray points). The "well-measured sample," with all emission lines in both spatial apertures measured with S/N > 1, is shown as blue circles. Open black circles indicate galaxies with an emission-line limit in at least one of the apertures. The "full sample" of galaxies (well-measured and limits) contains about 31% of the CLEAR galaxies at this redshift. The red line is the star formation mass sequence from Whitaker et al. (2012) shown in Equation (2). Right: distribution of redshifts from our selected sample of CLEAR galaxies in the range $0.6 < z < 1.3$, with blue indicating the well-measured sample and black the full sample including limits, compared to the complete CLEAR data set in the range $0.6 < z < 1.3$ (gray histogram).

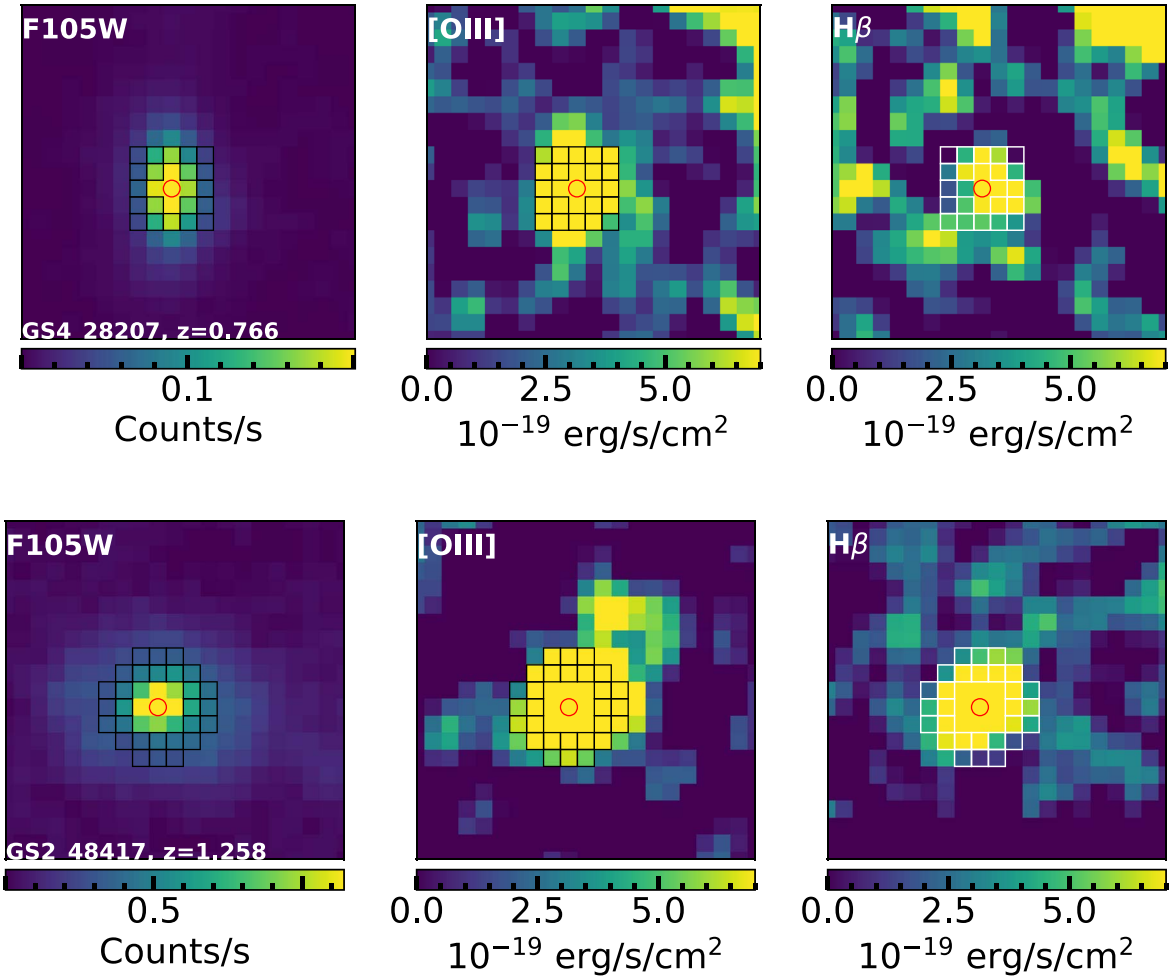

Figure 2. The top and bottom panels show examples of a large and small galaxy and their outer-aperture regions. Top: small galaxy with $R_{50} < 2\farcs5$ with an outer-aperture region of 20 pixels shown as boxes. Bottom: large galaxy with $R_{50} > 2\farcs5$ with an outer-aperture region of 28 pixels shown as boxes. Left: F105W direct images. Middle: [O III] emission-line maps. Right: Hβ emission-line maps. The pixel scale is $0\farcs1$ in all panels, corresponding to ~1 kpc at the redshift of these galaxies. The center of these galaxies is the F105W centroid.

Table 1
Sample

ID	Global Ratio	Inner Ratio	Outer Ratio	$\log(M_\star/M_\odot)$	z	log(SFR)	R_{50}
GN1_36795	4.42 ± 1.14	1.74 ± 1.45	1.99 ± 0.93	9.87	1.22	1.58	0.39
GN1_38027	2.50 ± 0.69	1.00 ± 0.50	2.06 ± 2.14	9.39	0.98	0.18	0.27
GN1_37494	2.31 ± 0.55	0.69 ± 0.51	1.08 ± 0.29	9.54	1.02	0.59	0.52
GN1_37031	0.84 ± 0.15	0.32 ± 0.24	0.28 ± 0.31	9.76	1.06	1.08	0.58
GN1_37567	2.88 ± 0.40	3.05 ± 1.21	7.80 ± 7.55	9.63	1.18	0.96	0.29
GN1_37812	2.08 ± 0.84	0.70 ± 0.74	0.72 ± 0.50	9.72	0.78	1.20	0.55
GN1_37691	4.46 ± 1.15	0.84 ± 0.59	3.12 ± 1.93	9.49	1.15	0.47	0.40
GN1_37700	1.65 ± 0.40	1.37 ± 0.47	1.09 ± 0.67	9.88	1.04	0.84	0.15
GN1_37053	1.44 ± 0.23	2.74 ± 2.89	1.17 ± 0.42	8.87	1.04	0.74	0.32
GN1_37750	12.21 ± 4.00	6.03 ± 1.56	3.55 ± 1.56	8.43	1.23	0.66	0.05

Note. The [O III]/Hβ ratios for the galaxies in the sample, measured from the global profile (e.g., integrated over the whole galaxy), in the inner central pixel and outer aperture. Other columns indicate the stellar mass, redshift, SFR, and effective radius of the galaxies. Only a portion of this table is shown here to demonstrate its form and content. A machine-readable version of the full table is available.

(This table is available in its entirety in machine-readable form.)

Table 2
Well-measured Binned Data

$\log(M_\star/M_\odot)$	$\log(M_\star/M_\odot)_{\rm Med}$	$\log(\rm SFR)_{\rm Med}$	$N_{\rm gal}$	Global Ratio	Inner Ratio	Outer Ratio	Spatial Difference
8.34–9.01	8.83	0.16 ± 0.01	10	0.60 ± 0.01	0.37 ± 0.03	0.36 ± 0.05	0.02 ± 0.05
	8.86	0.61 ± 0.03	11	0.77 ± 0.01	0.79 ± 0.02	0.43 ± 0.06	0.37 ± 0.07
9.02–9.32	9.18	0.33 ± 0.01	10	0.66 ± 0.02	0.44 ± 0.03	0.54 ± 0.06	-0.11 ± 0.07
	9.20	0.80 ± 0.02	11	0.56 ± 0.02	0.34 ± 0.07	0.47 ± 0.00	-0.13 ± 0.12
9.33–9.59	9.42	0.47 ± 0.02	10	0.44 ± 0.02	0.29 ± 0.05	0.23 ± 0.07	0.06 ± 0.09
	9.49	0.77 ± 0.03	11	0.63 ± 0.02	0.17 ± 0.04	0.31 ± 0.06	-0.15 ± 0.07
9.60–9.79	9.69	0.52 ± 0.01	11	0.31 ± 0.02	-0.02 ± 0.04	0.20 ± 0.04	-0.22 ± 0.06
	9.66	1.10 ± 0.02	11	0.53 ± 0.01	0.33 ± 0.03	0.18 ± 0.07	0.16 ± 0.08
9.82–10.99	9.96	0.85 ± 0.01	10	0.17 ± 0.01	-0.02 ± 0.03	0.08 ± 0.02	-0.09 ± 0.03
	10.33	1.96 ± 0.02	11	0.41 ± 0.01	0.05 ± 0.04	0.37 ± 0.04	-0.32 ± 0.05

Note. Median [O III]/Hβ emission-line ratios for galaxies in bins of stellar mass and SFR using only the well-measured galaxies, shown as a filled blue histogram in Figures 3 and 4. We first break our data into five stellar mass bins, and we use the median SFR of the mass bin to create two sub-bins representing high and low SFRs. The uncertainty of the median is given for the ratio and spatial difference measurements. The low- (high-) SFR bins are depicted as stars (hexagons) in Figures 5, 6, and 10.

ratios across the spatial profile of each galaxy. We begin by defining the "center" of the galaxies, i.e., where we expect to find a central AGN, to be the middle of the pixel of the photometric centroid of the F105W image. The pixel scale of both the images and the 2D grism spectra is $0\farcs1$ pixel^{-1}, which for the redshift range of this sample corresponds to approximately 1 kpc pixel^{-1}. This resolution is sufficient such that the ionization from a central AGN can be spatially distinguished from the more extended emission associated with distributed star formation.

In order to characterize the emission lines from the extended star-forming region of the galaxy, we define an outer-aperture region outside of the central pixel. The number of pixels chosen depends on the size of the galaxy as determined from the half-light radii (R_{50}) from the F125W CANDELS images (van der Wel et al. 2014). For galaxies with $R_{50} > 2\farcs5$, we selected a set of 28 pixels symmetrically around the center pixel from the extended regions of the galaxy. Smaller galaxies use a similar but slightly smaller shape with only 20 pixels. In both cases, we leave a gap of at least 1 pixel between the central pixel and the extended region in order to minimize blending between the regions of emission and avoid correlated fluxes from neighboring pixels in the drizzled WFC3 data. The geometry of the extended region pixel selection from larger and compact objects is demonstrated in Figure 2.

The extended [O III]/Hβ ratio is calculated as the median [O III]/Hβ ratios in the outer aperture. We choose the median as a statistically robust measure of the extended emission-line flux, since many galaxies contain pixels with lower S/N measurements and/or outlier flux caused by contamination. Use of the median allows the outlier pixels to be ignored in the aperture measurement for the galaxy. We also calculated the outer-aperture emission-line flux using the mean, weighted mean, weighted mean with outlier rejection, and weighted median. These other methods generally resulted in similar flux values but tended to be more affected by outliers or had larger uncertainties than using the simple median.

Our sample's integrated inner- and outer-aperture ratio measurements are shown in Table 1 along with the stellar mass, redshift, SFR, and effective radius of the galaxies.

Of our sample of 218 galaxies, 112 have at least one limit in a flux measurement from the inner or outer regions, usually from the Hβ emission line, resulting in a limit in the [O III]/Hβ spatial difference. We define a "well-measured sample" of the 106 galaxies that have both [O III] and Hβ detected at S/N > 1 in both apertures, as well as a "full sample" of the 218 galaxies

Table 3
Binned Data Including Limits

$\log(M_\star/M_\odot)$	$\log(M_\star/M_\odot)_{\rm Med}$	$\log({\rm SFR})_{\rm Med}$	$N_{\rm gal}$	Global Ratio	Inner Ratio	Outer Ratio	Spatial Difference
8.34–8.99	8.81	-0.01 ± 0.01	21	0.53 ± 0.01	0.39 ± 0.03	0.28 ± 0.04	0.11 ± 0.05
	8.85	0.59 ± 0.01	22	0.69 ± 0.01	0.76 ± 0.03	0.39 ± 0.05	0.37 ± 0.06
9.00–9.34	9.19	0.28 ± 0.01	21	0.60 ± 0.02	0.49 ± 0.03	0.40 ± 0.05	0.09 ± 0.06
	9.19	0.77 ± 0.01	22	0.61 ± 0.01	0.37 ± 0.05	0.50 ± 0.07	-0.13 ± 0.09
9.36–9.58	9.47	0.33 ± 0.01	22	0.57 ± 0.02	0.36 ± 0.06	0.38 ± 0.06	-0.02 ± 0.08
	9.49	0.86 ± 0.02	23	0.60 ± 0.01	0.41 ± 0.06	0.39 ± 0.06	0.02 ± 0.09
9.59–9.79	9.68	0.59 ± 0.01	22	0.34 ± 0.01	-0.02 ± 0.03	0.23 ± 0.03	-0.25 ± 0.04
	9.68	1.21 ± 0.02	22	0.36 ± 0.03	0.24 ± 0.03	0.15 ± 0.05	0.09 ± 0.06
9.82–10.99	9.91	0.94 ± 0.02	22	0.28 ± 0.01	0.05 ± 0.03	0.19 ± 0.03	-0.14 ± 0.04
	10.34	1.95 ± 0.02	22	0.25 ± 0.02	0.05 ± 0.04	0.04 ± 0.05	0.01 ± 0.06

Note. Median [O III]/Hβ emission-line ratios for galaxies in bins of stellar mass and SFR for the entire sample, including galaxies with limits in the emission lines. This uses the binning method that was used in Table 2. The low- (high-) SFR bins are depicted as stars (hexagons) in Figures 5, 6, and 10.

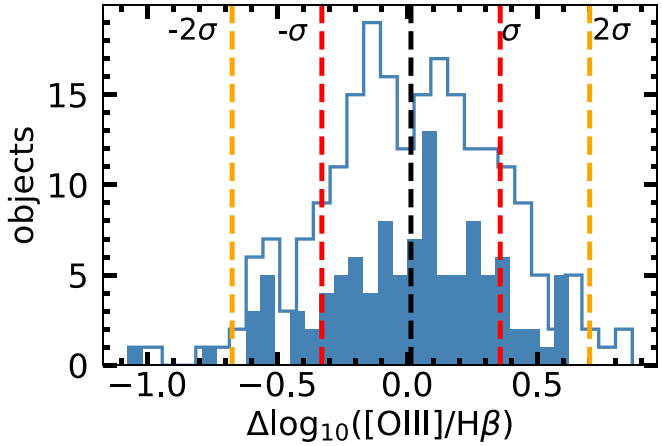

Figure 3. Distribution of the inner minus the outer [O III]/Hβ ratio. The filled histogram represents the distribution of galaxies that have well-measured [O III] and Hβ fluxes in both their central pixel and outer aperture. The open histogram represents the distribution of the full sample, including galaxies that have an upper limit in one or more of the central or outer [O III] or Hβ fluxes. The median [O III]/Hβ spatial difference is 0.0147, the standard deviation is 0.3428, and most galaxies have a spatial difference that is consistent with zero.

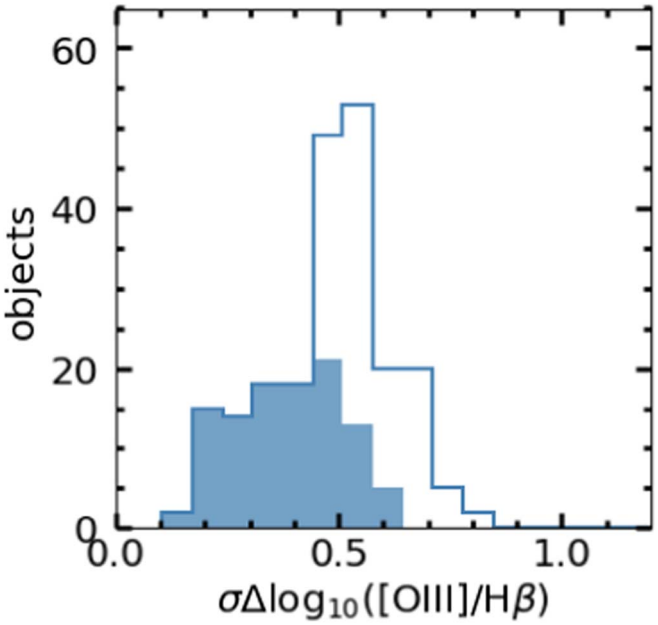

Figure 4. Distribution of the uncertainty in the inner minus the outer [O III]/Hβ ratio. The filled histogram represents the distribution of galaxies that have well-measured [O III] and Hβ fluxes in both their central pixel and outer aperture. The open histogram represents the distribution of the full sample, including galaxies using a limit of [O III] or Hβ. As expected, galaxies with well-measured fluxes have smaller uncertainties. In general, most of the line ratios have large uncertainties compared to the measurements.

that includes limits in emission lines in at least one of the spatial apertures.

4.1. Binned Line Ratio Profiles

We mitigate the large uncertainties and limits of individual galaxies from both samples by putting them into five bins based on their stellar mass, with each bin containing about 21–22 and 43–45 galaxies, respectively. We then split each mass bin into two sub-bins of high- and low-Hβ SFRs using the median Hβ SFR of each bin, giving us a total of 10 bins with 10 ± 1 and 22 ± 1 galaxies in each, respectively. This will show if there are any relations between the [O III]/Hβ spatial difference and stellar mass and SFR.

We then calculate the median stellar mass and SFR of each bin. The [O III]/Hβ spatial difference for each bin is created by taking the median emission-line fluxes from both apertures to create the ratios. The median mass, SFR, emission-line ratio, and spatial difference for each bin are shown in Tables 2 and 3 for the well-measured and full samples.

5. Results

We define the [O III]/Hβ spatial difference as the difference between the log([O III]/Hβ) ratio in the inner pixel and the ratio in the outer region. Figures 3 and 4 show the distributions of the [O III]/Hβ spatial difference and [O III]/Hβ spatial difference uncertainty, respectively. In these diagrams, the filled blue histogram is the distribution of galaxies with well-measured emission-line fluxes in both the inner and outer apertures. The open blue histogram is the distribution of the entire sample, including galaxies with limits in at least one emission-line flux.

Figure 3 shows that most of the objects have measured [O III]/Hβ spatial differences close to zero, although there is large scatter. Much of this scatter is likely due to the large [O III]/Hβ spatial difference uncertainties seen in Figure 4;

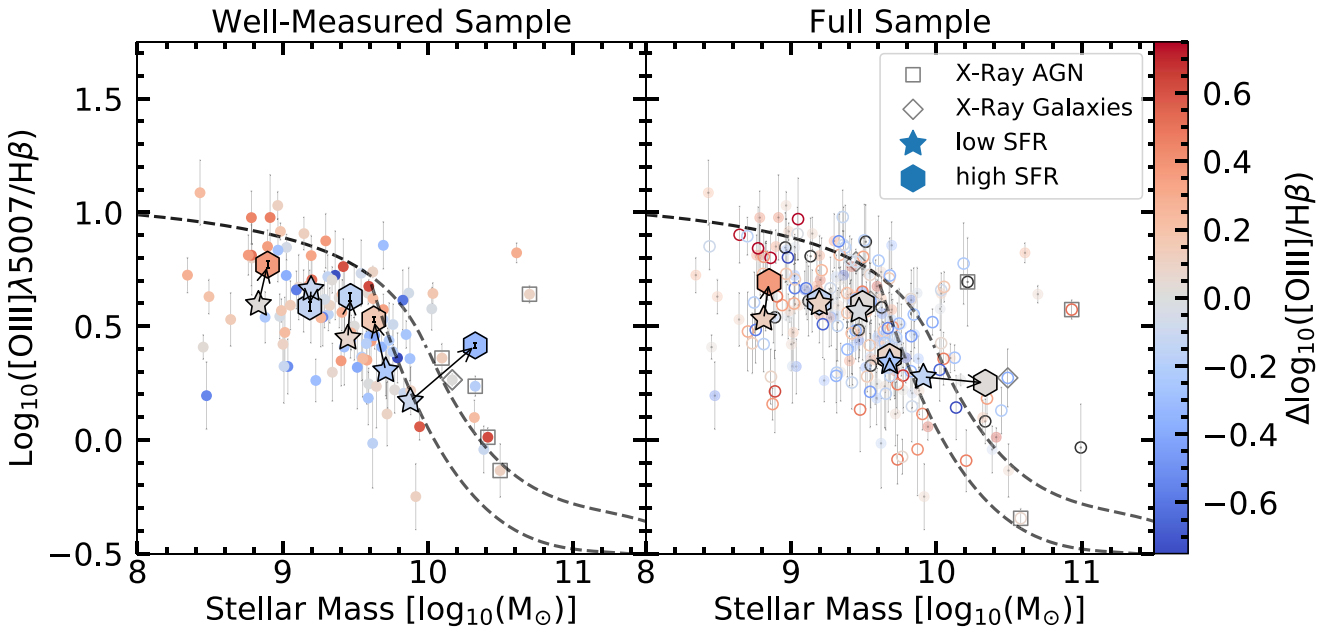

Figure 5. The MEx diagram of the galaxies in our sample. The integrated [O III]/Hβ ratios are given on the vertical axis, and the points are shaded by the inner minus the outer [O III]/Hβ ratio. Left: galaxies with well-measured [O III]/Hβ spatial differences in both inner and outer apertures. The binned high and low SFR shown as hexagons and stars are the same as stated in Table 2; each pair of low and high SFR for a certain mass is connected by a black arrow. Right: our entire sample, including galaxies with limits in emission-line flux in the inner and/or outer regions. The open circles show galaxies with an upper or lower limit in the spatial difference. The gray open circles are galaxies that have limits in both the inner and outer regions and are statistically unconstrained. The stars and hexagons are the ratios of the galaxies binned by mass and SFR described in Table 3. The objects identified via X-rays are shown with open squares (AGN) and diamonds (galaxies). The black dashed line represents the empirical division between star-forming galaxies (below the line) and galaxies with AGN (above the line) for galaxies at this redshift (Juneau et al. 2014). The median bins also have uncertainties, but they are too small to be seen in this diagram. In both panels, galaxies with lower stellar mass tend to have higher integrated [O III]/Hβ ratios and a higher nuclear [O III]/Hβ ratio.

only 29 galaxies, 13% of the sample, have a [O III]/Hβ spatial difference uncertainty less than 0.3 dex. The median uncertainty for the entire sample is 0.5 dex (open histogram), with a median [O III]/Hβ spatial difference uncertainty of 0.38 dex for the well-measured sample of galaxies with no limits in inner/outer emission-line fluxes (filled blue histogram).

5.1. General Emission-line Ratio Properties

We place the two samples of galaxies on a MEx diagram using the Juneau et al. (2014) AGN/star-forming line shown in Figure 5, with all of the well-measured galaxies in the left panel and the full sample in the right panel. Also shown are the objects in the sample that are X-ray sources and with X-ray emission classified as coming from AGN or star-forming galaxies (Xue et al. 2016; Luo et al. 2017). The open circles in the right panel represent upper or lower limits for the [O III]/Hβ spatial difference as shown by the color bar. The gray open circles in the right panel are galaxies that have the same type of limit in both the inner and outer regions, making the spatial difference unconstrained. The large stars and hexagons are the ratios of the galaxies binned by mass and SFR described in Table 3. Our sample is offset from the AGN/star-forming line because of aperture differences between our grism measurements and the SDSS sample used in Juneau et al. (2014); see Trump et al. (2015) for more details on typical SDSS aperture losses.

Figure 5 shows that low-mass galaxies prefer higher [O III]/Hβ in their nucleus. This will be further investigated in Section 6.2 For both samples, the binned medians show no significant difference in the [O III]/Hβ spatial difference between the high and low SFRs. For both samples, the bins, similar to individual galaxies, indicate that low stellar mass galaxies marginally prefer nuclear ionization (higher [O III]/Hβ in the nucleus), while high stellar mass galaxies tend to have neutral or slightly off-nuclear ionization (higher [O III]/Hβ in the extended region).

The X-ray AGN are identified in massive galaxies due to the well-known stellar mass bias for X-ray detection (Aird et al. 2012). The most luminous known X-ray AGN do not have large [O III]/Hβ spatial differences, as the AGN in these galaxies are likely so bright that the emission from the AGN narrow-line region overwhelms the entire host galaxy's star formation emission lines. These X-ray AGN are generally identified in traditional BPT diagrams because they have high integrated [O III]/Hβ ratios. This effect was also seen in the simulations of Bridge et al. (2016).

Figure 6 further investigates the relationship between [O III]/Hβ spatial differences and galaxy stellar mass. For both samples, there is no strong trend between the resolved [O III]/Hβ and stellar mass, as there is a large range of [O III]/Hβ spatial differences across the sample. There is a marginal preference for low-mass galaxies to have nuclear ionization. In Sections 6.2 and 6.3, we further investigate the galaxies that deviate from zero [O III]/Hβ spatial difference.

5.2. Spatially Resolved [OIII]/Hβ Ratios with Galaxy Properties

We now investigate how the spatially resolved emission-line spatial difference is affected by a galaxy's classification as a star-forming or AGN galaxy, as well as how the [O III]/Hβ spatial difference correlates to galaxy stellar mass, SFR, size, and redshift.

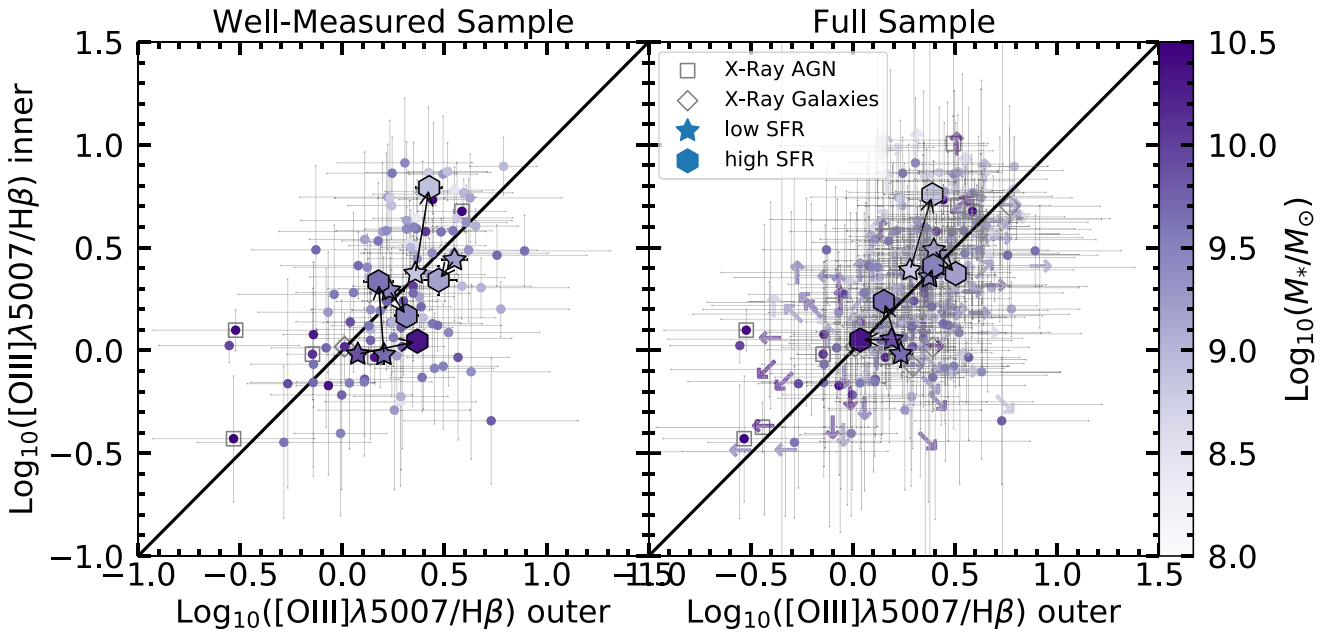

Figure 6. Inner [O III]/Hβ vs. outer [O III]/Hβ color-coded by stellar mass for both the well-measured sample (left) and the full sample (right). The arrows represent limits in the measured line ratios, with diagonal arrows representing limits in both axes. The median bin uncertainties are too small to be seen. The black line is the 1:1 ratio between the inner and outer regions. The stars and hexagons are from the bins described in Tables 2 and 3. Due to the large uncertainties, most of our sample overlaps are consistent with zero [O III]/Hβ gradient; however, we will focus on the galaxies that show significant differences between their nuclear and off-nuclear [O III]/Hβ ratios. Both the median bins and individual galaxies have a preference for low stellar mass galaxies to have higher [O III]/Hβ in the nucleus.

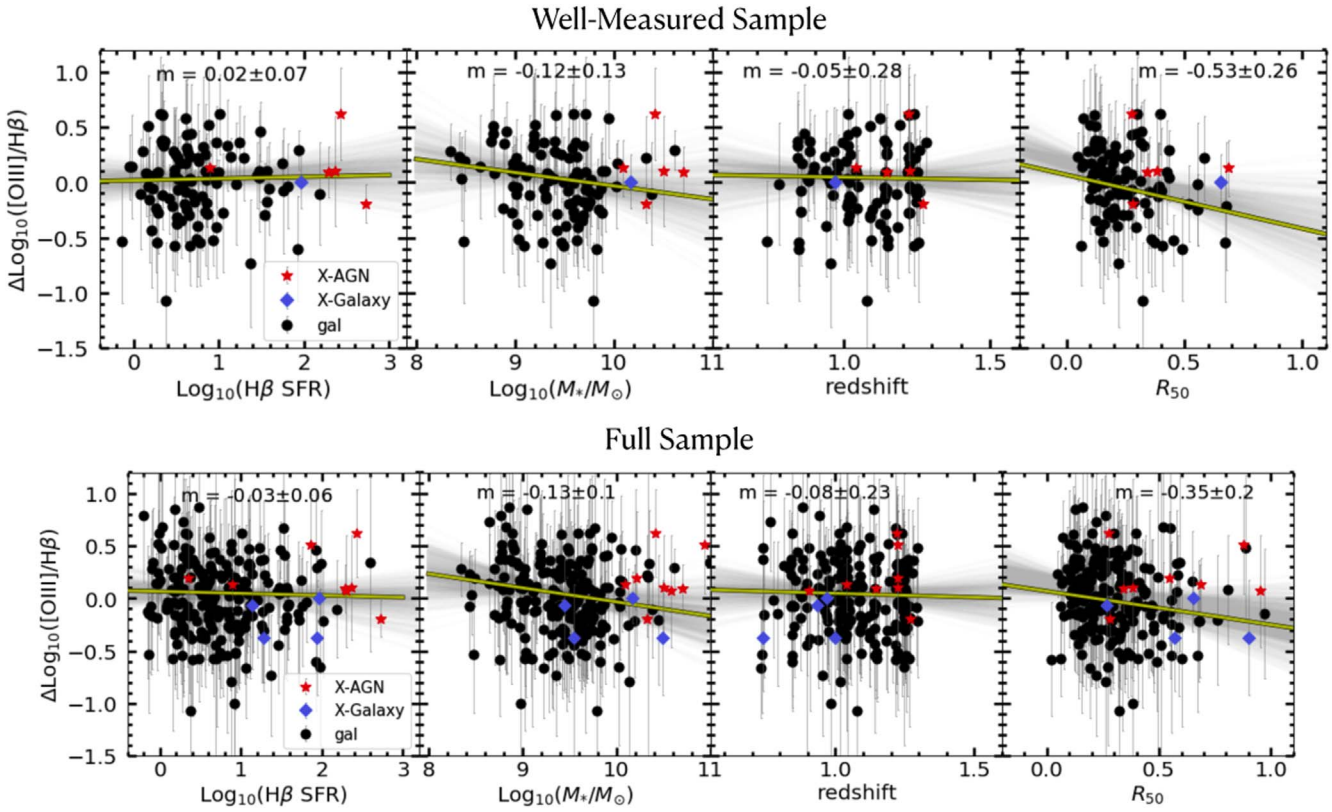

Figure 7. Relationships of [O III]/Hβ spatial difference with galaxy SFR, stellar mass, redshift, and effective radius. The X-ray AGN and X-ray galaxies are shown as red stars and blue diamonds, respectively. Each panel has a yellow linear regression best-fit line fit to the galaxies excluding X-ray AGN, with its slope showing the strength of the relationship. The top row uses only the well-measured galaxies in our sample, while the bottom row is the full sample that includes galaxies with limits. The [O III]/Hβ spatial difference has marginal anticorrelations with effective radius in both rows and a marginal anticorrelation with stellar mass for the full sample.

Figure 7 investigates the relationship between the line ratio spatial difference and galaxy properties, with X-ray AGN and X-ray galaxies shown as red stars and blue diamonds, respectively. We carry out a linear regression fit to the sample excluding the X-ray AGN and plot the best-fit line in yellow with its slope and uncertainty reported in each

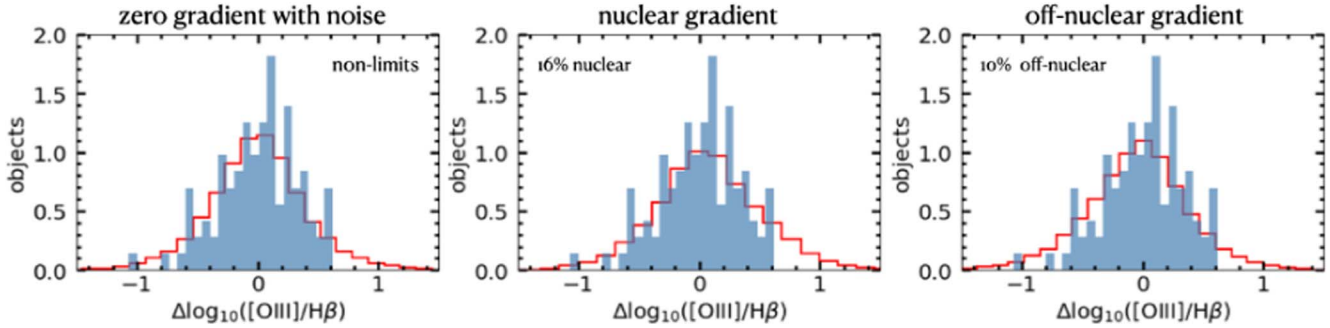

Figure 8. In each panel, we compare the distribution of emission-line ratio spatial differences in our well-measured galaxies (blue histogram) to simulated data sets (red line). In the left panel, we show a simulated distribution with zero emission-line spatial difference with noise. An Anderson–Darling test returns $p > 0.25$, showing that the distributions are consistent. In the middle panel, we increase the fraction of galaxies with higher nuclear emission-line spatial differences (+0.5 dex) until the Anderson–Darling test is $p < 0.05$; this occurs where 16% of the galaxies have spatial differences (with 0.5 dex higher [O III]/Hβ in the nucleus). The right panel repeats the test but using −0.5 dex spatial differences, where we find that the Anderson–Darling test is $p < 0.05$ when 10% of the galaxies show off-nuclear spatial differences (where the [O III]/Hβ ratio is 0.5 dex higher in the outskirts of the galaxies).

panel. The well-measured galaxies are shown in the top row, whereas the full sample is shown in the bottom row. In all of the panels, X-ray AGN have a preference for higher [O III]/Hβ in the nucleus, which we would expect for an AGN ionizing the central gas. The average [O III]/Hβ spatial difference of X-ray AGN is 0.12 dex, while the rest of the galaxy population has a [O III]/Hβ spatial difference of −0.01 dex. X-ray galaxies, on the other hand, have similar [O III]/Hβ spatial differences to other galaxies of the same stellar mass.

In Figure 7, we find that the [O III]/Hβ spatial difference does not have a relationship with Hβ SFR or redshift in both samples, as shown in the first and third panels. In the full sample, there is a marginal (1.3σ) anticorrelation between the [O III]/Hβ spatial difference and stellar mass, which was also observed in Figure 5. For both samples, there is also a marginal (1.7σ–2σ) relationship between the line ratio spatial difference and galaxy size, with higher nuclear ionization in smaller galaxies. The relationships of the line ratio spatial difference with stellar mass and size are likely related due to the known correlation between galaxy mass and radius (van der Wel et al. 2014; Mowla et al. 2019; Yang et al. 2021).

6. Discussion

6.1. An Intrinsic Population of Galaxies with Higher Nuclear Ionization

Figure 3 shows a broad distribution of measured [O III]/Hβ spatial differences, and Figure 7 shows that nuclear ionization is marginally preferred in X-ray AGN, low-mass galaxies, and small galaxies. But it is unclear how much of the distribution of measured spatial differences is due to noise or the intrinsic galaxy population. To further investigate this, we compare our measurements with different models for the underlying distribution.

Figure 8 shows galaxies with well-measured line ratio spatial differences as the blue histogram and compares its distribution to different models, shown by red lines. In the left panel, our model depicts a distribution of galaxies with zero intrinsic spatial difference and noise drawn from the observed uncertainties. An Anderson–Darling test returned a p-value of >0.25, indicating that the model is consistent with being drawn from the same parent distribution as the observed galaxies. In the middle and right panels, we start adding galaxies with higher nuclear or off-nuclear [O III]/Hβ ratios (a spatial difference of +0.5 and −0.5 dex, respectively) until an Anderson–Darling test finds $p < 0.05$ such that the distributions are no longer consistent with the same parent distribution. We choose ±0.5 dex because, as shown in Figure 4, our well-measured spatial difference sample (filled blue histogram) uncertainty extends to 0.5 dex. The middle panel indicates that up to 16% of the galaxies can have nuclear [O III]/Hβ that is 0.5 dex higher than the outer region before the model has a different parent distribution from the subsample. In the right panel, the model distributions indicate that up to 10% of the galaxies can have off-nuclear ionization before it has a different distribution from the subsample. This shows that even though the distribution of well-measured galaxies is consistent with noise, there is still room for a small fraction of the galaxies to have nonzero differences between [O III]/Hβ in their nucleus and extended region.

We repeat this analysis again but this time with a subsample of galaxies that have the lowest $\delta\Delta\log_{10}$([O III]/Hβ), shown in Figure 9. This leaves us with 30 galaxies in our blue histograms with a spatial difference uncertainty of less than 0.3 dex. This low-uncertainty sample covers a similar range of redshifts, stellar masses, and Hβ SFRs as the full and well-measured samples. An Anderson–Darling test between the samples returns a p-value greater that 0.05 for all three of these galaxy properties, indicating that they come from the same parent distribution as our full and well-measured samples. The left panel shows a model with zero intrinsic spatial difference using the same uncertainties as the observations. In this case, an Anderson–Darling test indicates that model is not a good description of the data, with $p = 0.01$. This indicates that, at least among galaxies with the smallest uncertainties in the line ratio profiles, there is a population of galaxies with intrinsically higher nuclear [O III]/Hβ that cannot be entirely explained by noise. The right panel shows that our sample can be modeled by at least 6% of the galaxies having nuclear [O III]/Hβ that is 0.5 dex higher than the outer region. The best-measured galaxies are statistically inconsistent with all galaxies having a flat [O III]/Hβ profile, and reproducing the observations requires 6% of the galaxies to have 0.5 dex higher nuclear [O III]/Hβ.

Meanwhile, in the larger population, we find that we can fit strong [O III]/Hβ nuclear ionization (0.5 dex) in up to 16% of the galaxies. Since the two samples have the same galaxy properties and an Anderson–Darling test indicating they are drawn from the same parent distribution, our investigation

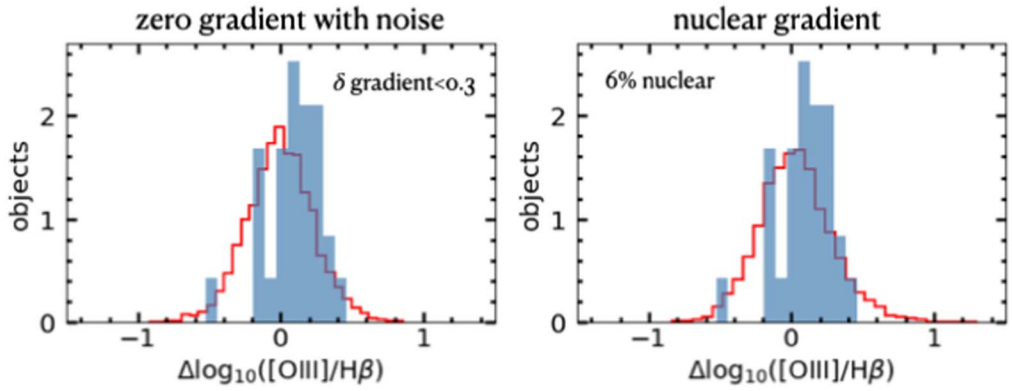

Figure 9. In each panel, we compare the distribution of emission-line ratio spatial differences in our galaxies with a $\delta\Delta\log_{10}([\mathrm{O\,III}]/\mathrm{H}\beta)$ under 0.3 dex (blue histogram) to simulated data sets (red line). In the left panel, we show a simulated distribution with zero emission-line spatial differences with noise. An Anderson–Darling test returns $p = 0.01$, showing that the distributions are inconsistent. In the right panel, we increase the fraction of galaxies with strong emission-line spatial differences (+0.5 dex) until the Anderson–Darling test is $p > 0.05$; this occurs where 6% of the galaxies have spatial differences (with stronger O III/Hβ in the nucleus). This tells us that the off-nuclear ionization galaxies are more likely to just be caused by noise.

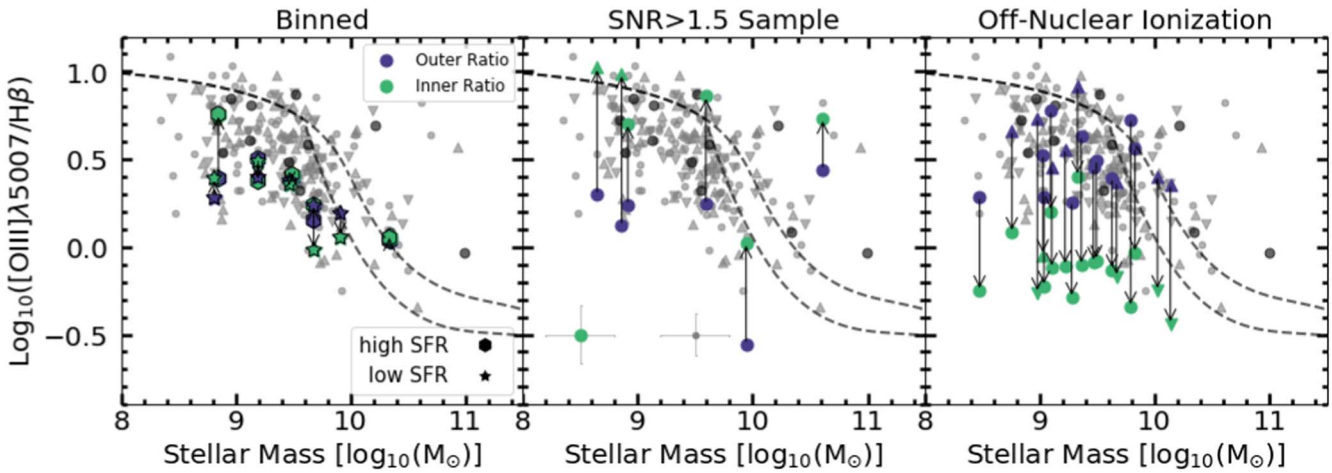

Figure 10. Left: inner and outer [O III]/Hβ ratios for galaxies binned by stellar mass and SFR as described by Table 3. Middle: six galaxies with [O III]/Hβ spatial distributions that are measured with at least 1.5σ certainty. All six of these galaxies have higher nuclear [O III]/Hβ ratios than their outer [O III]/Hβ ratios, suggesting higher nuclear ionization. All six of these galaxies are not X-ray detected in the deep CDF-S and CDF-N catalogs (Xue et al. 2016; Luo et al. 2017). Two of these galaxies have a lower limit in the inner ratio, meaning that the [O III]/Hβ spatial difference is also a lower limit. Right: 19 objects that have (∼0.5 dex) higher [O III]/Hβ ratios in their outer regions compared to their inner ratio.

implies that 6%–16% of the galaxies can have nuclear ionization that is 0.5 dex higher than their outer regions. As we used a p-value of 0.05, this 6%–16% fraction of galaxies with higher nuclear ionization roughly corresponds to a 95% confidence interval.

6.2. Nuclear Ionization and Low-luminosity AGN

In the previous subsection, we find that our sample is consistent with 6%–16% of the galaxies having higher nuclear [O III]/Hβ. In this subsection, we investigate individual galaxies that are candidates for having high nuclear ionization. The middle panel of Figure 10 shows the line ratio profiles of the six galaxies with positive [O III]/Hβ spatial differences detected with more than 1.5σ significance. Two of these galaxies have a lower limit in their inner [O III]/Hβ ratio, as shown by the triangles in Figure 10. The galaxies shown in the middle panel of Figure 10 have an average spatial difference of 0.6 dex, which is larger than the average X-ray AGN [O III]/Hβ spatial difference of 0.12 dex shown in Figure 7 and the AGN identification threshold of $\Delta\log([\mathrm{O\,III}]/\mathrm{H}\beta) = 0.1$ dex used in Bridge et al. (2016). The large difference between nuclear and extended [O III]/Hβ makes the six galaxies prime candidates to host low-luminosity AGN.

Figure 11 shows continuum (F105W), [O III], and Hβ images for two of the galaxies identified in the right panel of Figure 10. The last column marks the galaxy of interest in the distribution of SFR and stellar mass of the parent sample. Figure 11 gives an example of a low-mass and a high-mass galaxy, where both are extended in their continuum and Hβ images but have more compact [O III] emission. The detection of higher nuclear [O III]/Hβ emission-line ratios could indicate a low-luminosity and/or obscured AGN that is undetected by the deep X-ray observations (Xue et al. 2016; Luo et al. 2017).

Spatial differences in [O III]/Hβ can also be caused by nonflat metallicity gradients resulting in varying [O III]/Hβ ratios across the disks. Simons et al. (2021) showed that high stellar mass galaxies at redshifts $z \sim 1.5$ generally have flat metallicity profiles, while low stellar mass galaxies have lower metallicity in the center (higher [O III]/Hb in the center). This would cause higher [O III]/Hβ in the center; however, the spatial differences we measure are ∼0.5 dex over ∼2 kpc, while Simons et al. (2021) had gradients of ∼0.1 dex kpc^{-1}, so

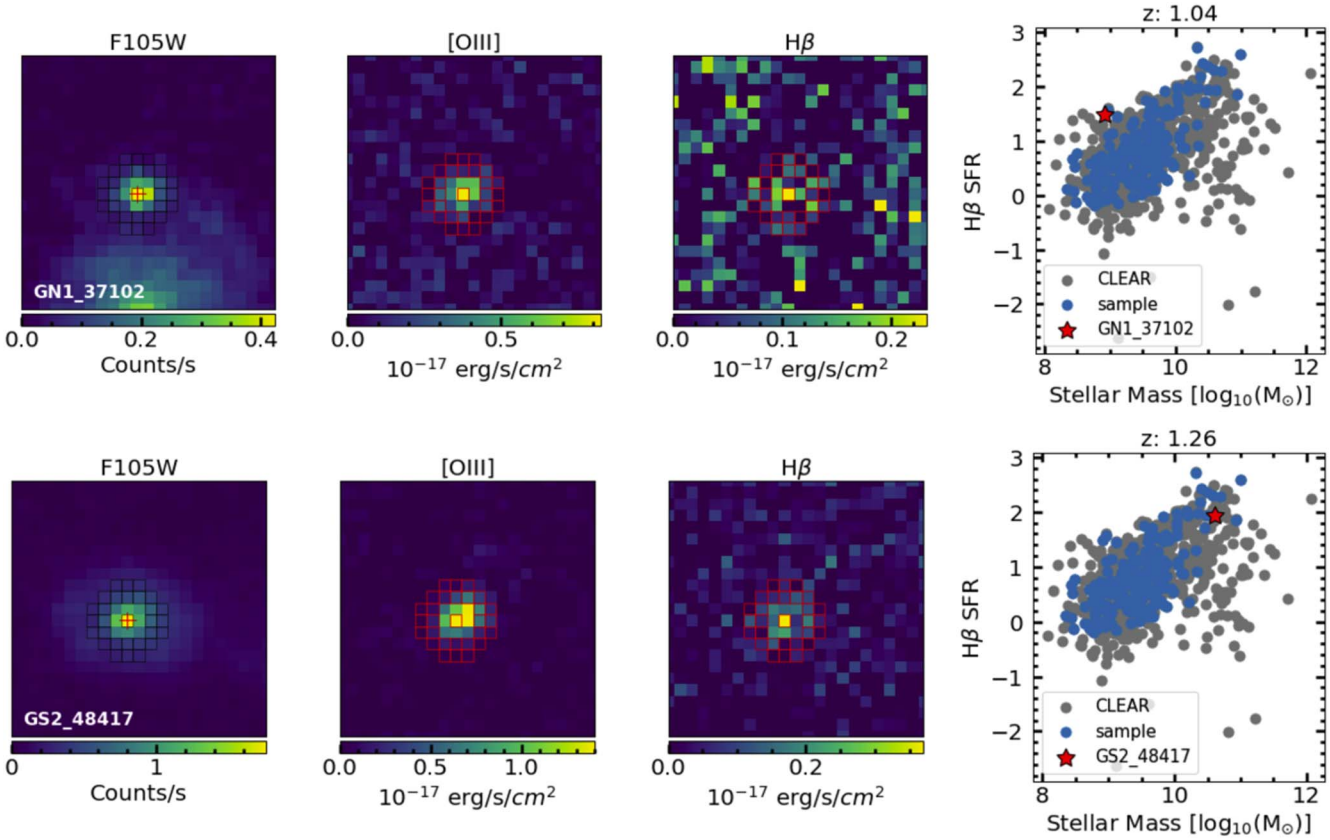

Figure 11. Two of the galaxies from the middle panel of Figure 10 that have spatial differences with S/N > 1.5 and indicate nuclear ionization. The first three columns show the F105W image, the [O III] emission-line map, and the Hβ emission-line map for each galaxy. The last column shows the SFR and stellar mass of the parent sample with the galaxy of interest highlighted as a red star. Both galaxies appear to have [O III] emission that is more compact than the continuum image and the Hb emission.

metallicity alone is unlikely to fully account for the elevated central [O III]/Hβ.

Using a similar analysis with stacked data from both CANDELS WFC3 and Chandra, Trump et al. (2011) found that it was likely that at least some of the galaxies in their sample of 28 objects contained weak AGN. Single-object studies have also been done; Wright et al. (2010) used the OSIRIS integral field spectrograph on the Keck Observatory to show that the nuclear region ($\sim$0.″2) of a $z \sim 1.5$ galaxy exhibits elevated [O III]/Hβ and [N II]/Hα ratios, which they posited is an indication of an embedded AGN. Our analysis finds six galaxies at $z \sim 1$ that show promise for hosting low-luminosity AGN.

6.3. Off-nuclear Ionization

Figure 5 and 6 show a wide range of line ratio profiles, including galaxies with higher [O III]/Hβ in their outer regions. Section 6.1 indicates that the observed high off-nuclear [O III]/Hβ ratios are consistent with flat [O III]/Hβ profiles and observational uncertainties. But the uncertainties are sufficiently large that the same analysis indicates that up to 10% of the galaxies might have off-nuclear ionization profiles with [O III]/Hβ that is 0.5 dex higher in galaxy outskirts than in galaxy centers. Such systems could be off-nuclear AGN or other sources of off-nuclear ionized gas. Evidence of off-nuclear massive black holes has been observed near the center of the Milky Way (Oka et al. 2017), and the discovery of extragalactic off-nuclear X-ray sources (e.g., Farrell et al. 2009; Jonker et al. 2010; Barrows et al. 2016) has lent credence to the idea that massive black holes exist at significant, 1 kpc or greater, distances from the centers of galaxies.

We investigate the possibility of off-nuclear AGN by investigating the line ratio maps of a sample of 19 objects that have ($\sim$0.5 dex) higher [O III]/Hβ ratios in their outer regions compared to their inner ratio, as shown in the right panel of Figure 10. Of the 19 galaxies, five of them cross the AGN/star-forming line, with an outer region indicating an AGN, while the central ratio stays in the star-forming region. Three of these five points also have a lower limit in their outer ratio measurement.

We first investigate if dust and/or orientation plays a role in causing higher off-nuclear [O III]/Hβ (Δ[O III]/Hβ < 0) using measurements of A_V attenuation and axis ratio from the compilation of Barro et al. (2019). Matching catalogs results in 196 galaxies from our sample, for which we show A_V and axis ratio measurements in Figure 12. From the left panel, we can see that the off-nuclear ionized galaxies do not have more dust attenuation that the rest of the sample. The right panel shows that the off-nuclear ionized galaxies are not preferentially viewed edge-on. An Anderson–Darling test between the off-nuclear sources and the full sample returns a p-value >0.25 for both dust attenuation and axis ratio, showing that the high off-nuclear ionization galaxies have the same distribution as the rest of the sample. This shows that high [O III]/Hβ ratios in galaxy outskirts are not preferentially produced by dust attenuation.

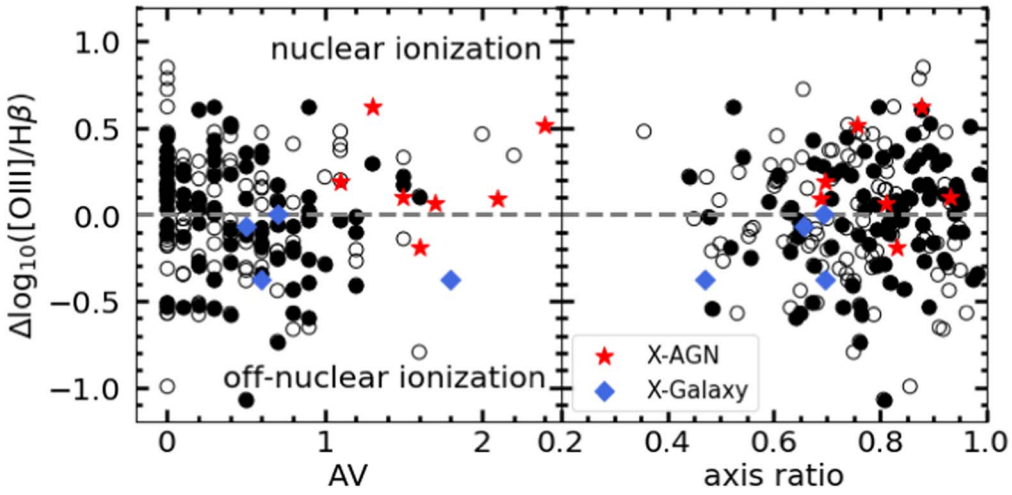

Figure 12. Left: [O III]/Hβ spatial difference, nuclear minus extended [O III]/Hβ, vs. dust attenuation. Right: spatial difference of [O III]/Hβ vs. the galaxy axis ratio. The X-ray AGN and X-ray galaxies are shown as red stars and blue diamonds, respectively. The filled black circles are well-measured galaxies, and the open circles are the galaxies with limits in the emission-line measurements. The off-nuclear ionization galaxies (negative $\Delta \log([\mathrm{O\,III}]/\mathrm{H}\beta)$) do not have more dust attenuation that the rest of the sample and also are not preferentially edge-on galaxies; this is seen in both the well-measured and limited galaxies. An Anderson–Darling test between the off-nuclear sources and the full sample returns a p-value >0.25, indicating that the high off-nuclear ionization galaxies are consistent with the same parent distribution as the rest of the sample.

We investigate the possibility of these galaxies hosting off-nuclear AGN by looking for clumping of off-nuclear [O III]/Hβ and/or continuum light at particular angles, as shown in Figure 13. The left panels show the F105W continuum image, the middle panels show the emission-line ratio of each pixel in the outer region verses the angle, and the right panels show the emission-line flux of each outer-region pixel color-coded by the angle. The middle and right panels show the median for the inner (outer) regions as a red (magenta) line or star, respectively, and limits are shown by triangles. Off-nuclear AGN might lead to a clump of high [O III]/Hβ ratio and high [O III] flux at a narrow range of angles. This is shown by simulations done by Bellovary et al. (2010) and Seepaul et al. (2022), which indicate that off-nuclear AGN can be detected if they retain a bound clump of both gas and stars.

These are the only two of the 19 galaxies with high off-nuclear [O III]/Hβ that have a preferred angle for higher [O III]/Hβ emission. If we also see more continuum light at that angle, this would give further indication of an off-nuclear AGN. However, we did not see this for either galaxy. The two galaxies shown in Figure 13 do show a peak [O III]/Hβ ratio at a particular angle in the middle panels, at $\sim 60^\circ$ for the top panel and $\sim 260^\circ$ for the bottom panel. But the continuum light in these galaxies does not have the same distribution and is instead concentrated at different angles (330° in the top galaxy and 150° in the bottom). The other 17 galaxies with high outer-region [O III]/Hβ do not show this kind of clumpiness; instead, the [O III]/Hβ is distributed over a wide range of angles.

The two galaxies examined in Figure 13 do not seem to be well described as off-nuclear AGN. These example galaxies could instead be ionized outflows, as there is no concentration of continuum light in the areas that are marked with high ionization. High outer-region [O III]/Hβ could indicate a metal-rich nucleus and metal-poor disk (commonly referred to as a "negative metallicity gradient"), as observed in some massive high-redshift galaxies (Wuyts et al. 2016). The number of galaxies with off-nuclear ionization is also fully consistent with the large uncertainty in the measured spatial differences, as indicated from our models of the intrinsic distribution of line ratio spatial differences.

7. Conclusions

We report measurements of resolved [O III]/Hβ line ratio profiles via HST/WFC3 G102 grism observations taken as part of the CLEAR survey. We measured [O III]/Hβ spatial differences by taking the center of the galaxy, defined by the photometric center of the F105W image, and subtracting the median of the [O III]/Hβ ratio in an annular extended region. We investigate the spatially resolved nature of this line ratio, and we summarize our results as follows.

1. The data binned by stellar mass and SFR in Figures 5 and 6 show that low stellar mass galaxies tend to have marginally higher nuclear [O III]/Hβ, whereas high stellar mass galaxies have flat spatial differences. The SFR of the galaxy is not correlated with the [O III]/Hβ spatial difference. A slight anticorrelation ($\sim 1.6\sigma$) between stellar mass and the [O III]/Hβ spatial difference is shown in Figure 7. This also shows an $\sim 2\sigma$ anticorrelation of effective radius with [O III]/Hβ spatial difference.
2. The X-ray AGN have a 0.1 dex higher nuclear [O III]/Hβ than the rest of the sample, as seen in Figure 7.
3. We compare toy models to the distribution of galaxies with well-measured spatial differences and galaxies with the lowest spatial difference uncertainty from our data set. From these toy models, Figures 8 and 9, we found that 6%–16% of the sample can include galaxies with higher nuclear [O III]/Hβ. The lower limit comes from the number of galaxies needed for the model to have a similar distribution to galaxies with the smallest spatial difference uncertainty, while the upper limit is from the number of galaxies before the model has a different distribution from galaxies with no limit in its spatial difference measurement.
4. Modeling the observations shows that galaxies with higher nuclear ionization are likely to exist, but the

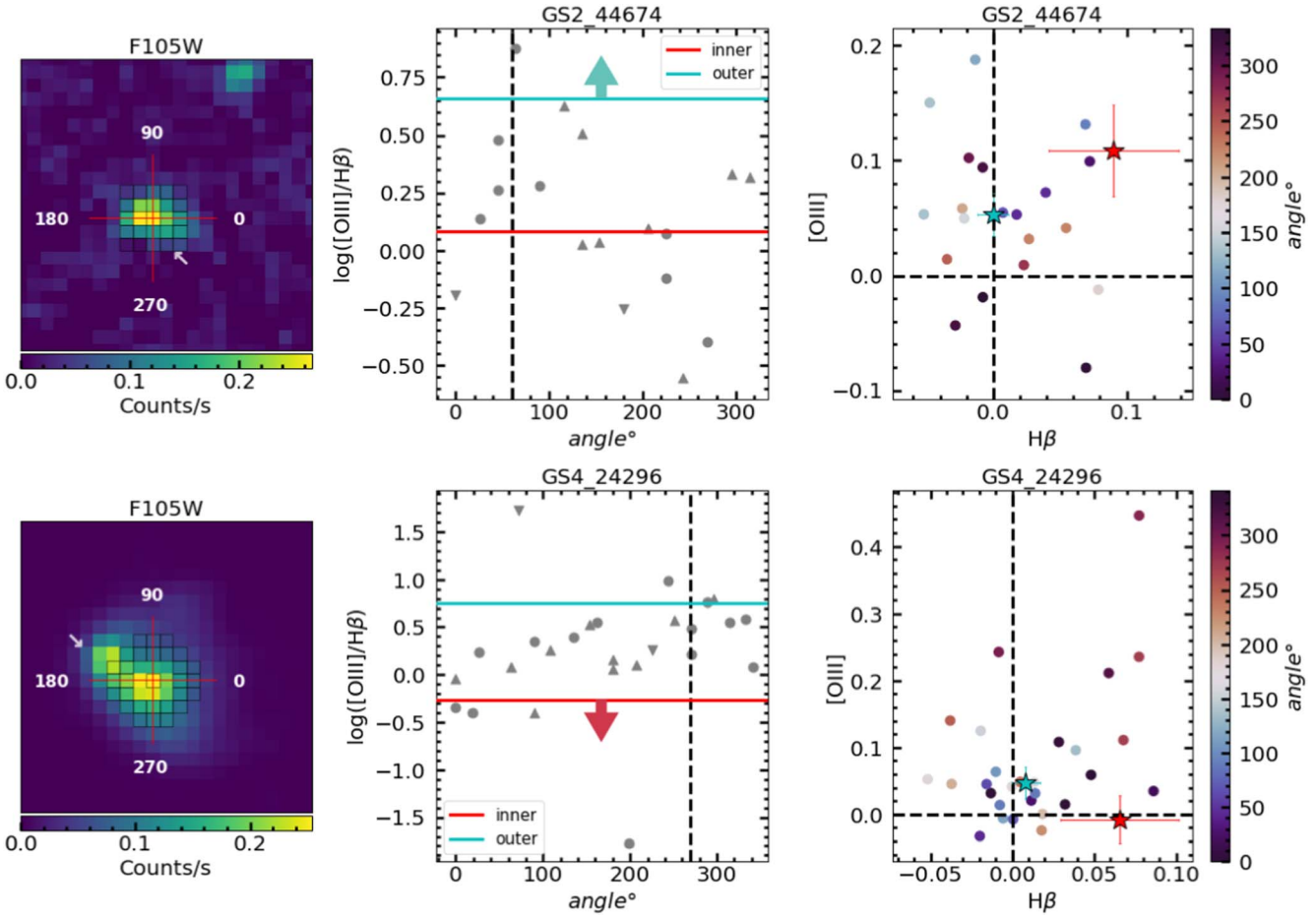

Figure 13. Two galaxies with higher off-nuclear [O III]/Hβ in the outskirts than in their centers. The left panels show the direct F105W image. The middle panels show the [O III]/Hβ of the outer-region pixels as a function of the angle shown in the left panel, with the inner-pixel ratio and median outer-pixel ratio shown as horizontal lines. The right panels show the outer-pixel [O III] and Hβ fluxes color-coded by angle, with limits in line fluxes and ratios shown by triangles. The inner-pixel ratio and median outer-pixel ratio are shown as red and blue stars, respectively. Both galaxies have an apparent preference for high [O III]/Hβ ratios at particular angles, shown by dashed vertical lines in the middle panels, that do not coincide with the continuum light in the direct image, indicated by white arrows in the left panels.

individual detections are marginal (only $\sim$1.5σ), as shown in Figure 10. One possible explanation for these galaxies is that they host a low-luminosity AGN in their nucleus that cannot be detected by X-rays or BPT diagrams.

5. We investigate the galaxies with the largest measured off-nuclear [O III]/Hβ ratios and find that they are generally consistent with observational noise. Two galaxies shown in Figure 13 have "clumpy" off-nuclear [O III] emission that is roughly orthogonal to the morphology of the continuum image and so is probably better described by an ionized gas cone than by off-nuclear AGN.

This work sheds light on the ensemble properties of $1 < z < 2$ galaxies, especially the conclusion that 6%–16% of the galaxies have considerably higher ($\sim$0.5 dex) nuclear [O III]/Hβ indicative of nuclear AGN that are missed by other methods. But the measurements of individual galaxies are limited by large uncertainties in the CLEAR data. A better understanding of individual galaxies, including searches for off-nuclear AGN or more nuanced ionization profiles, requires deeper data. This is available from HST/WFC3 grism data in FIGS and MUDF and will soon be available from JWST/NIRISS surveys like ngDEEP.

This work is based on data obtained from the Hubble Space Telescope through program No. GO-14227. Support for program GO-14227 was provided by NASA through a grant from the Space Telescope Science Institute, which is operated by the Association of Universities for Research in Astronomy, Inc., under NASA contract NAS5-26555. B.E.B. and J.R.T. acknowledge support from NSF grant CAREER-1945546 and NASA grant JWST-ERS-01345. J.S.B. acknowledges support from NASA/STScI grant HST-AR-15008.

Facility: HST (WFC3).

Software: `AstroPy` (Astropy Collaboration et al. 2013), `Matplotlib` (Hunter 2007), `NumPy` (van der Walt et al. 2011), `SciPy` (Jones et al. 2001), `grizli` (Brammer 2022), `eazy-py` (Brammer et al. 2008; Brammer 2021), `FSPS` (Conroy & Gunn 2010).

ORCID iDs

Bren E. Backhaus https://orcid.org/0000-0001-8534-7502
Joanna S. Bridge https://orcid.org/0000-0002-8584-1903
Jonathan R. Trump https://orcid.org/0000-0002-1410-0470
Nikko J. Cleri https://orcid.org/0000-0001-7151-009X
Casey Papovich https://orcid.org/0000-0001-7503-8482
Raymond C. Simons https://orcid.org/0000-0002-6386-7299

Ivelina Momcheva https://orcid.org/0000-0003-1665-2073
Benne W. Holwerda https://orcid.org/0000-0002-4884-6756
Zhiyuan Ji https://orcid.org/0000-0001-7673-2257
Intae Jung https://orcid.org/0000-0003-1187-4240
Jasleen Matharu https://orcid.org/0000-0002-7547-3385

References

Aird, J., Coil, A. L., Moustakas, J., et al. 2012, ApJ, 746, 90
Astropy Collaboration, Robitaille, T. P., Tollerud, E. J., et al. 2013, A&A, 558, A33
Backhaus, B. E., Trump, J. R., Cleri, N. J., et al. 2022, ApJ, 926, 161
Baldwin, J. A., Phillips, M. M., & Terlevich, R. 1981, PASP, 93, 5
Barro, G., Pérez-González, P. G., Cava, A., et al. 2019, ApJS, 243, 22
Barrows, R. S., Comerford, J. M., Greene, J. E., et al. 2016, ApJ, 829, 37
Bellovary, J. M., Governato, F., Quinn, T. R., et al. 2010, ApJL, 721, L148
Brammer, G. 2021, eazy-py, v0.5.2, Zenodo, doi:10.5281/zenodo.5012705
Brammer, G. 2022, grizli, v1.5.0, Zenodo, doi:10.5281/zenodo.1146904
Brammer, G., Pirzkal, N., McCullough, P., et al. 2014, Time-varying Excess Earth-glow Backgrounds in the WFC3/IR Channel, 2014-03STScI
Brammer, G., Ryan, R., & Pirzkal, N. 2015, Source-dependent master sky images for the WFC3/IR grisms WFC3, 2015-17STScI
Brammer, G. B., van Dokkum, P. G., & Coppi, P. 2008, ApJ, 686, 1503
Bridge, J. S., Zeimann, G. R., Trump, J. R., et al. 2016, ApJ, 826, 172
Buchner, J., Georgakakis, A., Nandra, K., et al. 2015, ApJ, 802, 89
Calzetti, D. 2001, PASP, 113, 1449
Cann, J. M., Satyapal, S., Abel, N. P., et al. 2019, ApJL, 870, L2
Cardelli, J. A., Clayton, G. C., & Mathis, J. S. 1989, ApJ, 345, 245
Chabrier, G. 2003, PASP, 115, 763
Cleri, N. J., Trump, J. R., Backhaus, B. E., et al. 2022, ApJ, 929, 3
Coil, A. L., Aird, J., Reddy, N., et al. 2015, ApJ, 801, 35
Conroy, C., & Gunn, J. E. 2010, FSPS: Flexible Stellar Population Synthesis, Astrophysics Source Code Library, ascl:1010.043
Estrada-Carpenter, V., Papovich, C., Momcheva, I., et al. 2019, ApJ, 870, 133
Estrada-Carpenter, V., Papovich, C., Momcheva, I., et al. 2020, ApJ, 898, 171
Farrell, S. A., Webb, N. A., Barret, D., Godet, O., & Rodrigues, J. M. 2009, Natur, 460, 73
Hickox, R. C., Jones, C., Forman, W. R., et al. 2009, ApJ, 696, 891
Hunter, J. D. 2007, CSE, 9, 90
Ji, Z., Giavalisco, M., Kirkpatrick, A., et al. 2022, ApJ, 925, 74
Jones, E., Oliphant, T., & Peterson, P. 2001, SciPy: Open Source Scientific Tools for Python, & Others, https://www.researchgate.net/publication/213877848_SciPy_Open_Source_Scientific_Tools_for_Python
Jones, M. L., Hickox, R. C., Black, C. S., et al. 2016, ApJ, 826, 12
Jonker, P. G., Torres, M. A. P., Fabian, A. C., et al. 2010, MNRAS, 407, 645
Juneau, S., Dickinson, M., Alexander, D. M., et al. 2011, ApJ, 736, 104
Juneau, S., Bournaud, F., Charlot, S., et al. 2014, ApJ, 788, 88
Jung, I., Papovich, C., Finkelstein, S. L., et al. 2022, ApJ, 933, 87
Kauffmann, G., Heckman, T. M., Tremonti, C., et al. 2003, MNRAS, 346, 1055
Kennicutt, R. C. 1998, ARA&A, 36, 189
Kennicutt, R. C., & Evans, N. J. 2012, ARA&A, 50, 531
Kewley, L. J., Dopita, M. A., Sutherland, R. S., Heisler, C. A., & Trevena, J. 2001, ApJ, 556, 121
Kewley, L. J., Nicholls, D. C., & Sutherland, R. S. 2019, ARA&A, 57, 511
Kewley, L. J., Zahid, H. J., Geller, M. J., et al. 2015, ApJL, 812, L20
Kimble, R. A., MacKenty, J. W., O'Connell, R. W., et al. 2008, Proc. SPIE, 7010, 70101E
Koekemoer, A. M., Faber, S. M., Ferguson, H. C., et al. 2011, ApJS, 197, 36
Lambrides, E. L., Chiaberge, M., Heckman, T., et al. 2020, ApJ, 897, 160
Lotz, J. M., Koekemoer, A., Coe, D., et al. 2017, ApJ, 837, 97
Luo, B., Brandt, W. N., Xue, Y. Q., et al. 2017, ApJS, 228, 2
Madau, P., & Dickinson, M. 2014, ARA&A, 52, 415
Maiolino, R., & Mannucci, F. 2019, A&ARv, 27, 3
Matharu, J., Papovich, C., Simons, R. C., et al. 2022, ApJ, 937, 16
Momcheva, I. G., Brammer, G. B., van Dokkum, P. G., et al. 2016, ApJS, 225, 27
Moran, E. C., Filippenko, A. V., & Chornock, R. 2002, ApJL, 579, L71
Mowla, L., van der Wel, A., van Dokkum, P., & Miller, T. B. 2019, ApJL, 872, L13
Nelson, E. J., van Dokkum, P. G., Brammer, G., et al. 2012, ApJL, 747, L28
Nelson, E. J., van Dokkum, P. G., Forster Schreiber, N. M., et al. 2016a, ApJ, 828, 27
Nelson, E. J., Dokkum, P. G. v., Momcheva, I. G., et al. 2016b, ApJL, 817, L9
Nelson, E. J., Tacchella, S., Diemer, B., et al. 2021, MNRAS, 508, 219
Oka, T., Tsujimoto, S., Iwata, Y., Nomura, M., & Takekawa, S. 2017, NatAs, 1, 709
Osterbrock, D. E., & Miller, J. S. 1989, Astrophysics of gaseous nebulae and active galactic nuclei (Sausalito, CA: Univ. Science Books)
Pagel, B. E. J., & Edmunds, M. G. 1981, ARA&A, 19, 77
Papovich, C., Simons, R. C., Estrada-Carpenter, V., et al. 2022, ApJ, 937, 22
Peimbert, M., Peimbert, A., & Delgado-Inglada, G. 2017, PASP, 129, 082001
Pirzkal, N., Malhotra, S., Ryan, R. E., et al. 2017, ApJ, 846, 84
Planck Collaboration, Ade, P. A. R., Aghanim, N., et al. 2016, A&A, 594, A13
Seepaul, B., Pacucci, F., & Narayan, R. 2022, MNRAS, 515, 2110
Simons, R. C., Papovich, C., Momcheva, I., et al. 2021, ApJ, 923, 203
Skelton, R. E., Whitaker, K. E., Momcheva, I. G., et al. 2014, ApJS, 214, 24
Steidel, C. C., Rudie, G. C., Strom, A. L., et al. 2014, ApJ, 795, 165
Tilvi, V., Pirzkal, N., Malhotra, S., et al. 2016, ApJL, 827, L14
Tremonti, C. A., Heckman, T. M., Kauffmann, G., et al. 2004, ApJ, 613, 898
Trump, J. R., Hsu, A. D., Fang, J. J., et al. 2013, ApJ, 763, 133
Trump, J. R., Weiner, B. J., Scarlata, C., et al. 2011, ApJ, 743, 144
Trump, J. R., Sun, M., Zeimann, G. R., et al. 2015, ApJ, 811, 26
van der Walt, S., Colbert, S. C., & Varoquaux, G. 2011, CSE, 13, 22
van der Wel, A., Franx, M., van Dokkum, P. G., et al. 2014, ApJ, 788, 28
Veilleux, S., & Osterbrock, D. E. 1987, ApJS, 63, 295
Whitaker, K. E., van Dokkum, P. G., Brammer, G., et al. 2012, ApJL, 754, L29
Wright, S. A., Larkin, J. E., Graham, J. R., et al. 2010, ApJ, 711, 1291
Wuyts, E., Wisnioski, E., Fossati, M., et al. 2016, ApJ, 827, 74
Xue, Y. Q., Luo, B., Brandt, W. N., et al. 2016, ApJS, 224, 15
Xue, Y. Q., Brandt, W. N., Luo, B., et al. 2010, ApJ, 720, 368
Yang, L., Roberts-Borsani, G., Treu, T., et al. 2021, MNRAS, 501, 1028
Zahid, H. J., Geller, M. J., Kewley, L. J., et al. 2013, ApJL, 771, L19